Controlled-Synthesis, Self-Assembly Behavior, and Surface-Dependent Optical Properties of High-Quality Rare-Earth Oxide Nanocrystals

Rui Si, Ya-Wen Zhang,* Huan-Ping Zhou, Ling-Dong Sun, and Chun-Hua Yan*

Beijing National Laboratory for Molecular Sciences, State Key Laboratory of Rare Earth Materials Chemistry and Applications, PKU-HKU Joint Laboratory in Rare Earth Materials and Bioinorganic Chemistry, Peking University, Beijing 100871, China

Single-crystalline and monodisperse cubic rare-earth (RE = La to Lu, Y) oxide nanocrystals (ultrathin nanoplates and nanodisks) have been synthesized via a nonhydrolytic approach in oleic acid (OA)/oleylamine (OM)/1-octadecene (ODE) using various rare-earth complexes, including acetylacetonate, benzoylacetonate, and acetate, as the precursors. The transformation from the complex precursors to RE_2O_3 was proposed to occur in two stages: first, the formation of rare-earth oleates by ligand exchange in solution, and second, the subsequent decomposition of the oleates into RE_2O_3 catalyzed by the base of OM. The selective adsorption of coordinating OA ligands onto specific crystal planes of cubic RE_2O_3 nanocrystals made them adopt a plate shape with the confined growth of {100} facets and/or a disk shape with the confined growth of {111} facets. Along with delicately tuning the polarity of the dispersant, the RE_2O_3 nanocrystals could be aligned to form "side-to-side" or "face-to-face" self-assembly nanoarrays on carbon-coated copper grids. With the developed synthetic method, we also obtained high-quality luminescent Y_2O_3:Eu ultrathin nanodisks, which displayed strong surface-dependent, highly pure red emissions that were due to selective incorporation of Eu^{3+} ions in the surface of the nanodisks.

Introduction

Since the 1990s, dispersible inorganic nanocrystals have attracted wide research interest not only because of their remarkable size-, shape-, or surface-dependent physical and chemical properties but also because of their powerful self-assembly capability of forming various superstructure patterns on diverse substrates in the application of nanodevices.[1−19]

For such nanomaterials to realize desirable and optimal properties, it remains a challenge to explore robust pathways and unify principles toward the systematic control of their size, shape, surface, and aggregation in various systems of metals,[1−4] metal oxides,[4−11] semiconductors,[4,12−15] and other compounds.[4,16−19] So far, the nonhydrolytic route (thermolysis of multiple metal complex precursors and their derivatives in exchangeable surfactant solutions) has been demonstrated as the most versatile one for the synthesis of high-quality (single-crystalline, monodisperse, well-shaped, and phase-pure) nanocrystals, including 0D dots and polyhedrons,[1−3,5−8,10,12−17,19] 1D rods and wires,[2,11,14,15,19] and 2D plates and disks.[9−11,18] Meanwhile, many groups have focused on the investigation of the self-assembled superlattice constructed by diverse surface-modified nanocrystals with capping ligands, from theoretical simulation to experimental fabrication and microscopic explanation of the monolayer and/or multilayer patterns.[20−29] Up until now, it has still been

* Corresponding author. Fax: +86-10-6275-4179. E-mail: yan@pku.edu.cn (C.-H.Y.).

(1) Sun, S. H.; Murray, C. B.; Weller, D.; Folks, L.; Moser, A. *Science* **2000**, *287*, 1989.
(2) Puntes, V. F.; Krishnan, K. M.; Alivisatos, A. P. *Science* **2001**, *291*, 2115.
(3) Jana, N. R.; Peng, X. *J. Am. Chem. Soc.* **2003**, *125*, 14280.
(4) Wang, X.; Zhuang, J.; Peng, Q.; Li, Y. *Nature* **2005**, *437*, 121.
(5) Park, J.; An, K.; Hwang, Y.; Park, J.-G.; Noh, H.-J.; Kim, J.-Y.; Park, J.-H.; Hwang, N.-M.; Hyeon, T. *Nat. Mater.* **2004**, *3*, 891.
(6) Yin, M.; O'Brien, S. *J. Am. Chem. Soc.* **2003**, *125*, 10180.
(7) Cheon, J.; Kang, N.-J.; Lee, S.-M.; Lee, J.-H.; Yoon, J.-H.; Oh, S. J. *J. Am. Chem. Soc.* **2004**, *126*, 1950.
(8) Seo, W. S.; Jo, H. H.; Lee, K.; Kim, B.; Oh, S. J.; Park, J. T. *Angew. Chem., Int. Ed.* **2004**, *43*, 1115.
(9) Cao, Y. C. *J. Am. Chem. Soc.* **2004**, *126*, 7456.
(10) Si, R.; Zhang, Y.-W.; You, L.-P.; Yan, C.-H. *Angew. Chem., Int. Ed.* **2005**, *44*, 3256.
(11) Yu, T.; Joo, J.; Park, Y. I.; Hyeon, T. *J. Am. Chem. Soc.* **2006**, *128*, 1786.
(12) Murray, C. B.; Norris, D. J.; Bawendi, M. G. *J. Am. Chem. Soc.* **1993**, *115*, 8706.
(13) Trindade, T.; O'Brien, P.; Zhang, X.-M. *Chem. Mater.* **1997**, *9*, 523.
(14) Peng, X.; Manna, L.; Yang, W.; Wickham, J.; Scher, E.; Kadavanich, A.; Alivisatos, A. P. *Nature* **2000**, *404*, 59.
(15) Monge, M.; Kahn, M. L.; Maisonnat, A.; Chaudret, B. *Angew. Chem., Int. Ed.* **2003**, *42*, 5321.
(16) Stouwdam, J. W.; van Veggel, F. C. J. M. *Nano Lett.* **2002**, *2*, 733.
(17) Kömpe, K.; Borchert, H.; Storz, J.; Lobo, A.; Adam, S.; Möller, T.; Haase, M. *Angew. Chem., Int. Ed.* **2003**, *42*, 5513.
(18) Zhang, Y.-W.; Sun, X.; Si, R.; You, L.-P.; Yan, C.-H. *J. Am. Chem. Soc.* **2005**, *127*, 3260.

(19) Mai, H.-X.; Zhang, Y.-W.; Si, R.; Yan, Z.-G.; Sun, L.-D.; You, L.-P.; Yan, C.-H. *J. Am. Chem. Soc.* **2006**, *128*, 6426.
(20) Motte, L.; Billoudet, F.; Pileni, M. P. *J. Phys. Chem.* **1995**, *99*, 16425.
(21) Kiely, C. J.; Fink, J.; Brust, M.; Bethell, D.; Schiffrin, D. J. *Nature* **1998**, *396*, 444.
(22) Wang, Z. L. *Adv. Mater.* **1998**, *10*, 13.
(23) Pohl, K.; Bartelt, M. C.; Figuera, J.; Bartelt, N. C.; Hrbek, J.; Hwang, R. Q. *Nature* **1999**, *397*, 238.
(24) Li, M.; Schnablegger, H.; Mann, S. *Nature* **1999**, *402*, 393.
(25) Whitesides, G. M.; Grzybowski, B. *Science* **2002**, *295*, 2418.
(26) Rabani, E.; Reichman, D. R.; Geissler, P. L.; Brus, L. E. *Nature* **2003**, *426*, 271.
(27) Jana, N. R. *Angew. Chem., Int. Ed.* **2004**, *43*, 1536.
(28) Shevchenko, E. V.; Talapin, D. V.; Murray, C. B.; O'Brien, S. *J. Am. Chem. Soc.* **2006**, *128*, 3620.
(29) Bigioni, T.-P.; Lin, X.-M.; Nguyen, T. T.; Corwin, E. I.; Witten, T. A.; Jaeger, H. M. *Nat. Mater.* **2006**, *5*, 265.

an urgent task for us to manipulate various self-organized patterns consisting of the nanobuilding blocks from 0D to 3D, achieve a better basic understanding of the observed complex self-assembly phenomena in a nanometric scale, and reveal the underlying fundamental theories and principles.

Recently, high-quality rare-earth functional nanocrystals have drawn great attention because of their unique physical and chemical properties and potential applications in the fields of luminescence devices, optical transmission, biochemical probes, medical diagnostics, and so forth.[4,9−11,16−19] For rare-earth oxides (RE_2O_3), one of the most important family of rare-earth materials, they were usually synthesized by pyrolyzing their oxysalt precipitates (oxalate, hydroxide, etc.) at high temperatures (>700 °C).[30] With this solid-state reaction method, it is quite hard to obtain monodisperse and nonaggregated RE_2O_3 nanoparticles. Recently, some groups tried to use the nonhydrolytic route to prepare size- and shape-controlled dispersible RE_2O_3 nanocrystals, taking various rare-earth complexes as the precursors.[9−11,31] For instance, Cao prepared single-unit-cell thick (1.1 nm) Gd_2O_3 square nanoplates from gadolinium acetate hydrate in oleic acid/oleylamine at 320 °C and observed their intriguing self-assembly capability of forming a side-to-side superlattice on the TEM grids.[9] Also using the acetate precursor but under different solvent composition and reaction temperatures, Hyeon et al. synthesized uniform rectangular-shaped Sm_2O_3 nanowires and nanoplates with a single-unit-cell thickness (1.1 nm).[11] By thermolysis of rare-earth benzoylacetonate complexes in oleic acid/oleylamine, our group demonstrated the general synthesis of dispersible rare earth oxides nanocrystals (nanopolyhedra, ultrathin nanoplates, and nanodisks), which exhibited striking self-assembly capability into large area nanoarrays.[10] Particularly, the Eu_2O_3 ultrathin nanodisks showed interesting optical properties related to a surface effect.[10]

In this article, we will report on the controlled synthesis of high-quality RE_2O_3 nanocrystals (ultrathin nanoplates and nanodisks) via the thermolysis of various rare-earth complexes (acetylacetonates, benzoylacetonates, and acetates) in the mixed solvent of oleic acid (OA)/oleylamine (OM)/1-octadecene (ODE). The mechanisms for the nanocrystal synthesis and the shape evolution involved are proposed on the basis of the characterization results. By tuning the polarity of the dispersant, we can align the 2D nanoplates and nanodisks to form side-to-side and face-to-face self-assembly nanoarrays, which are discussed by considering the interparticle interaction modes in the dispersant. By the developed synthetic route, we have also prepared high-quality luminescence Y_2O_3:Eu ultrathin nanodisks. They have shown strong surface-dependent optical properties.

Experimental Section

1. Materials. RE_2O_3 (RE = La to Lu, Y), oleic acid (OA; 90%, Alpha), oleylamine (OM; >80%, Acros), 1-octadecene (ODE;

>90%, Acros), acetylacetone (Hacac, A. R. grade), 1-benzoylacetone (HBA, Acros), nitric acid (HNO_3, A. R. grade), ammonia ($NH_3 \cdot H_2O$, A. R. grade), acetic acid (HAc, >99.5%), oxalic acid ($H_2C_2O_4$, A. R. grade), sodium hydroxide (NaOH, >96%), absolute ethanol (C_2H_6O, >99.7%), cyclohexane (C_6H_{12}, >99.5%), triethylamine (TEA, >99.0%), and commercial Y_2O_3:Eu (5 at %) powders were used as received.

2. Synthesis of REL_3 Complexes. Rare-earth acetylacetonate ($RE(acac)_3$, RE = La to Lu, Y) was prepared according to the following procedure: RE_2O_3 (10 mmol) was dissolved in 40 mL of deionized water by adding HNO_3 to obtain $RE(NO_3)_3$. Hacac (80 mmol) was dissolved in 40 mL of deionized water by adding $NH_3 \cdot H_2O$ (80 mmol). The above two solutions were mixed together under stirring, and a dilute $NH_3 \cdot H_2O$ solution was then added into the mixed solution dropwise (final pH: 6−7). The stock solution was further aged at room temperature for 8 h and then filtered. The precipitate was collected, washed by deionized water, and dried in a vacuum at 60°C overnight. The C, H contents in the products were consistent with the calculated values (Table 1S). The synthesis of yttrium benzoylacetonate ($Y(BA)_3$) was according to our previous method.[10] For yttrium acetate ($Y(Ac)_3$), Y_2O_3 (10 mmol) was dissolved in refluxing HAc. The stock solution was filtered and slowly evaporated in air on a heater until a white powder appeared. For yttrium hydroxide ($Y(OH)_3$), $Y(NO_3)_3$ (20 mmol) was added into a diluted $NH_3 \cdot H_2O$ solution. The stock solution was stirred for 1 h and then filtered. The white precipitate was washed by deionized water and dried in air at 80 °C overnight. For yttrium oxalate ($Y_2(C_2O_4)_3$), $Y(NO_3)_3$ (20 mmol) was mixed with an aqueous solution of oxalic acid. The stock solution was stirred for 1 h and then filtered. The white precipitate was washed by deionized water and dried in air at 80 °C overnight. For yttrium oleate ($Y(OA)_3$), OA (15 mmol) and NaOH (15 mmol) were dissolved in ethanol (100 mL) under heating. $Y(NO_3)_3$ (5 mmol) was then added into the above solution. The stock solution was stirred for 1 h and then filtered. The colorless gel was washed by ethanol and dried in a vacuum at 70 °C overnight. The yields for these rare-earth complexes were between 40 and 80%.

3. Synthesis of RE_2O_3 (RE = La to Lu, Y) Nanocrystals. The synthesis was carried out using standard oxygen-free procedures. For a typical preparation, $Y(acac)_3$ (0.5 mmol) was added into a 10 mL mixed solvent of OA/OM/ODE with a volume ratio of 2/3/5 in a three-necked flask at room temperature. The stock solution was bubbled in an Ar atmosphere for 20 min and then vacuumed at ca. 100 °C for 30 min to remove adsorbed water. The flask was then heated to 310 °C at a rate of 20 °C min^{-1} and maintained at this temperature for 1 h under an Ar atmosphere. When the reaction completed, an excess amount (∼ 40 mL) of ethanol was poured into the solution at ca. 70 °C. This solution was separated by centrifugation, and the products were collected. The as-precipitated nanocrystals were washed by ethanol for several times and then dried in air at 70 °C overnight. The yield of the as-dried nanocrystals was more than 80%. The as-precipitated nanocrystals could be redispersed in nonpolar solvents (e.g., cyclohexane).

4. Synthesis of Y_2O_3:Eu (5 at %) Nanocrystals. The synthetic procedure was the same as that used to synthesize Y_2O_3 nanocrystals, except that quantitative $Y(acac)_3$ (0.475 mmol) and Eu-$(acac)_3$ (0.025 mmol) were taken as the precursors and added into ta mixture of 10 mL of OA/OM/ODE solvent (Table 1) in a three-necked flask at room temperature. A nanoparticle reference was prepared via the coprecipitation route in aqueous solution from stoichiometric $Y(NO_3)_3$ and $Eu(NO_3)_3$, using dilute $NH_3 \cdot H_2O$ as the precipitator. The as-precipitated powder was separated by filtration, dried at 80 °C in air overnight, and then calcined at 800 °C for 4 h in still air.

(30) Hussein, G. A. M. *J. Anal. Appl. Pyrolysis* **1996**, *37*, 111.
(31) Wang, H.; Uehara, M.; Nakamura, H.; Miyazaki, M.; Maeda, H. *Adv. Mater.* **2005**, *17*, 2506.

Table 1. Size, Shape, and Synthetic Conditions (including type (REL$_3$) and amount (M) of the precursor, composition (OA/OM/ODE) and volume (V) of the solvent, reaction temperature (T), and time (t)) of the Cubic ($Ia3$) RE$_2$O$_3$ (RE = La to Lu, Y) Nanocrystals

product	size (nm), shape	REL$_3$	M (mmol)	OA/OM/ODE	V (mL)	T (°C)	t (h)
La$_2$O$_3$	5−15 nm nanoplate	La(acac)$_3$	0.2	1/4/0	15	330	1
Pr$_2$O$_3$	11.1 (1.7^a), nanoplate	Pr(acac)$_3$	0.2	3/5/0	15	330	1
Nd$_2$O$_3$	7.6 (0.8), nanoplate	Nd(acac)$_3$	0.2	3/5/0	15	330	1
Sm$_2$O$_3$	20.0 (1.7), nanodisk	Sm(acac)$_3$	0.2	3/5/0	15	310	1
Eu$_2$O$_3$	20.3 (1.6), nanodisk	Eu(acac)$_3$	0.2	3/5/0	15	310	1
Gd$_2$O$_3$	9.3 (1.0), nanodisk	Gd(acac)$_3$	0.1	3/4.5/2.5	10	310	1
Tb$_2$O$_3$	12.4 (1.2), nanodisk	Tb(acac)$_3$	0.1	3/4.5/2.5	10	310	1
Dy$_2$O$_3$	11.8 (1.1), nanodisk	Dy(acac)$_3$	0.1	3/4.5/2.5	10	310	1
Ho$_2$O$_3$	10.6 (0.9), nanodisk	Ho(acac)$_3$	0.5	2/3/5	10	310	1
Er$_2$O$_3$	10.3 (0.8), nanodisk	Er(acac)$_3$	0.5	2/3/5	10	310	1
Tm$_2$O$_3$	11.0 (1.0), nanodisk	Tm(acac)$_3$	0.5	2/3/5	10	310	1
Yb$_2$O$_3$	13.8 (1.1), nanodisk	Yb(acac)$_3$	0.5	2/3/5	10	310	1
Lu$_2$O$_3$	11.6 (1.0), nanodisk	Lu(acac)$_3$	0.5	2/3/5	10	310	1
Y$_2$O$_3$	13.3 (1.1), nanodisk	Y(acac)$_3$	0.5	2/3/5	10	310	1
	10.6 (1.1), nanodisk	Y(BA)$_3$	0.5	2/3/5	10	310	1
	17.5 (1.6), nanodisk	Y(Ac)$_3$	0.5	2/3/5	10	310	1
	11.7 (1.2), nanodisk	Y(OH)$_3$	0.5	2/3/5	10	310	1
	10.5 (1.8), nanodisk	Y(acac)$_3$	0.2	2/3/5	10	310	1
	16.3 (2.0), nanodisk	Y(acac)$_3$	0.5	4/6/0	10	310	1
	11.2 (1.2), nanodisk	Y(acac)$_3$	0.5	1/4/5	10	310	1
	28.8 (2.3), nanodisk	Y(acac)$_3$	0.5	2.5/2.5/5	10	310	1
	12.1 (1.2), nanodisk	Y(acac)$_3$	0.5	2/3/5	10	330	1
	9.4 (0.9), nanodisk	Y(acac)$_3$	0.5	2/3/5	10	310	0.5
	16.7 (1.3), nanodisk	Y(acac)$_3$	0.5	2/3/5	10	310	2
Y$_2$O$_3$:Eu	16.0 (1.4), nanodisk	Y(acac)$_3$	0.475	3/4.5/2.5	10	310	1
		Eu(acac)$_3$	0.025				
	23.2 (2.0), nanodisk	Y(acac)$_3$	0.475	4/6/0	10	310	1
		Eu(acac)$_3$	0.025				

^{a} The standard deviation statistic from at least 100 nanocrystals.

5. Surface Modification of Y$_2$O$_3$ Nanocrystals. Hacac (5 mmol) and TEA (5 mmol) were mixed together. The as-precipitated Y$_2$O$_3$ nanocrystals (∼ 0.1 mmol) were then added to the above solution. After being stirred for a while, the solution became transparent and could be further mixed with ethanol without becoming cloudy.

6. Instrumentation. The thermogravimetry (TG) runs were performed with a Universal V2.60 TA instrument at a heating rate of 5 °C min⁻¹ from room temperature to 700 °C, using a-Al$_2$O$_3$ as a reference. Gas chromatography mass spectrometry (GCMS) tests on a GCQ (Finnigan-MAT, USA) instrument were carried out to investigate the reaction mechanism. The injection of the gaseous species (ca. 3 μL) was performed at 280 °C. The initial column temperature was held at 80 °C and then ramped at 40 °C min⁻¹ to 280 °C. Byproducts were identified by a SCAN technique according to their m/z peaks and quantified by the use of software with single ion monitoring (SIM) mode from each specific m/z peak abundance. Elemental analysis was carried out on an Elementary Vario EL (Germany) system. Powder X-ray diffraction (XRD) patterns of the as-dried nanocrystals were recorded on a Rigaku D/MAX-2000 diffractometer (Japan) with a slit of 1° at a scanning rate of 1° min⁻¹, using Cu−K$_\alpha$ radiation (λ = 1.5406 Å). The lattice constant was calculated by using the least-squares method. Nanoparticle size and shape were examined by a JEOL-200CX (Japan) transmission electron microscope (TEM) operated at 160 kV or a Hitachi-H9000 (Japan) high-resolution TEM (HRTEM) operated at 300 kV. Samples for TEM analysis were prepared by drying one drop of the nanocrystal dispersion on amorphous carbon-coated copper grids. The dynamic light scattering (DLS) experiments were carried out at 25 °C with ALV SLS-5022F laser light scattering spectroscopy and a Spectra-Physics 2017 Ar laser (514.5 nm wavelength). The scattering angle was 90°, and the intensity autocorrelation functions were analyzed by using the methods of CONTIN and cumulants. For the DLS measurements, the as-prepared nanocrystal dispersion was purified by a ultrathin filter (D < 0.2 μm) in advance. Room-temperature fluorescence spectra were recorded on a Hitachi F-4500 spectrophotometer equipped with a 150 W Xe-arc lamp at a fixed bandpass of 0.2 nm with the same instrument

parameters (2.5 nm for excitation split, 2.5 nm for emission split and 700 V for PMT voltage), with different samples of the as-dried Y$_2$O$_3$:Eu powders. The site-selective excitation spectra were measured at 77 K using a SPEX1403 double-grating monochromator and a R955 photomultiplier with a rhodamine 6G laser pumped by the YAG:Nd laser. The scan rate was fixed at 0.2 nm s⁻¹ for both excitation and emission spectra.

Results and Discussion

1. Characterization of RE$_2$O$_3$ Nanocrystals. Through serial condition-dependent experiments, the optimal conditions (type and concentration of precursor, solvent composition, reaction temperature, and time) were achieved for the synthesis of high-quality RE$_2$O$_3$ nanocrystals, as summarized in Table 1. All the as-dried RE$_2$O$_3$ (RE = La to Lu, Y) nanocrystals are of the body-centered cubic (bcc) structure (space group: $Ia3$), which can be identified from the XRD patterns of some typical samples shown in Figure 1 and the Supporting Information, Figure 1S. The calculated lattice constant a is 11.28(6) Å for La$_2$O$_3$ (JCPDS 22-369), 11.05-(2) Å for Sm$_2$O$_3$ (JCPDS 15-813), 11.01(2) Å for Eu$_2$O$_3$ (JCPDS 34-392), 10.83(1) Å for Tb$_2$O$_3$ (JCPDS 23-1418), 10.63(1) Å for Ho$_2$O$_3$ (JCPDS 44-1268), 10.56(2) Å for Er$_2$O$_3$ (JCPDS 8-50), 10.45(1) Å for Yb$_2$O$_3$ (JCPDS 18-1463), and 10.63(1) Å for Y$_2$O$_3$ (JCPDS 25-1200).

Figure 2 and the Supporting Information, Figure 2S, show the TEM images of the as-obtained RE$_2$O$_3$ nanocrystals, which are of narrow size distribution (see Table 1). The as-obtained RE$_2$O$_3$ nanocrystals were observed to exhibit two types of shapes: ultrathin square nanoplates for those from La$_2$O$_3$ to Nd$_2$O$_3$, and ultrathin nanodisks for those from Sm$_2$O$_3$ to Lu$_2$O$_3$, including Y$_2$O$_3$ (see lower insets in images a and f of Figure 2). Panels a−f of Figure 2 show the TEM images of 11.1 ± 1.7 nm Pr$_2$O$_3$ nanoplates, 7.6 ± 0.8 Nd$_2$O$_3$
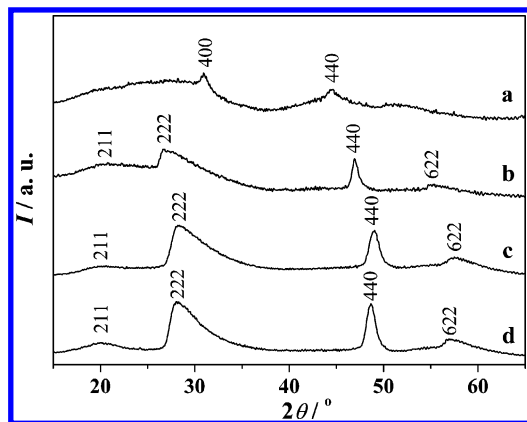
Figure 1. XRD patterns of the as-dried RE$_2$O$_3$ nanocrystals: (a) La$_2$O$_3$, (b) Eu$_2$O$_3$, (c) Er$_2$O$_3$, and (d) Y$_2$O$_3$.

nanoplates, 20.0 ± 1.7 nm Sm$_2$O$_3$ nanodisks, 20.3 ± 1.6 nm Eu$_2$O$_3$ nanodisks, 10.6 ± 0.9 nm Ho$_2$O$_3$ nanodisks, and 13.3 ± 1.1 nm Y$_2$O$_3$ nanodisks, respectively. Both the

nanoplates and the nanodisks can self-assemble into two types of nanoarrays via the side-to-side or the face-to-face formation (typically see Figure 2a,b,d,e).

The HRTEM images inserted in images a and f of Figure 2 display the side surface of a standing single-crystalline Pr$_2$O$_3$ nanoplate and a standing single-crystalline Y$_2$O$_3$ nanodisk, respectively. The Pr$_2$O$_3$ nanoplate shows a confined growth of {100} facets (see the shown (400) planes in the upper inset of Figure 2a)[10] and has a thickness of 1.0 ± 0.1 nm, close to the lattice constant of the bcc Pr$_2$O$_3$ unit cell. The Y$_2$O$_3$ nanodisk displays a confined growth of {111} facets (see the shown (222) planes in the upper inset of Figure 2f)[10] and shows a thickness of 2.0 ± 0.2 nm, corresponding to the size of six (222) layers in bcc Y$_2$O$_3$.

2. Condition Optimization for the Synthesis of RE$_2$O$_3$ Nanocrystals. To obtain high-quality RE$_2$O$_3$ nanocrystals, we have selected Y$_2$O$_3$ as an example to systematically investigate the effects of various experimental parameters
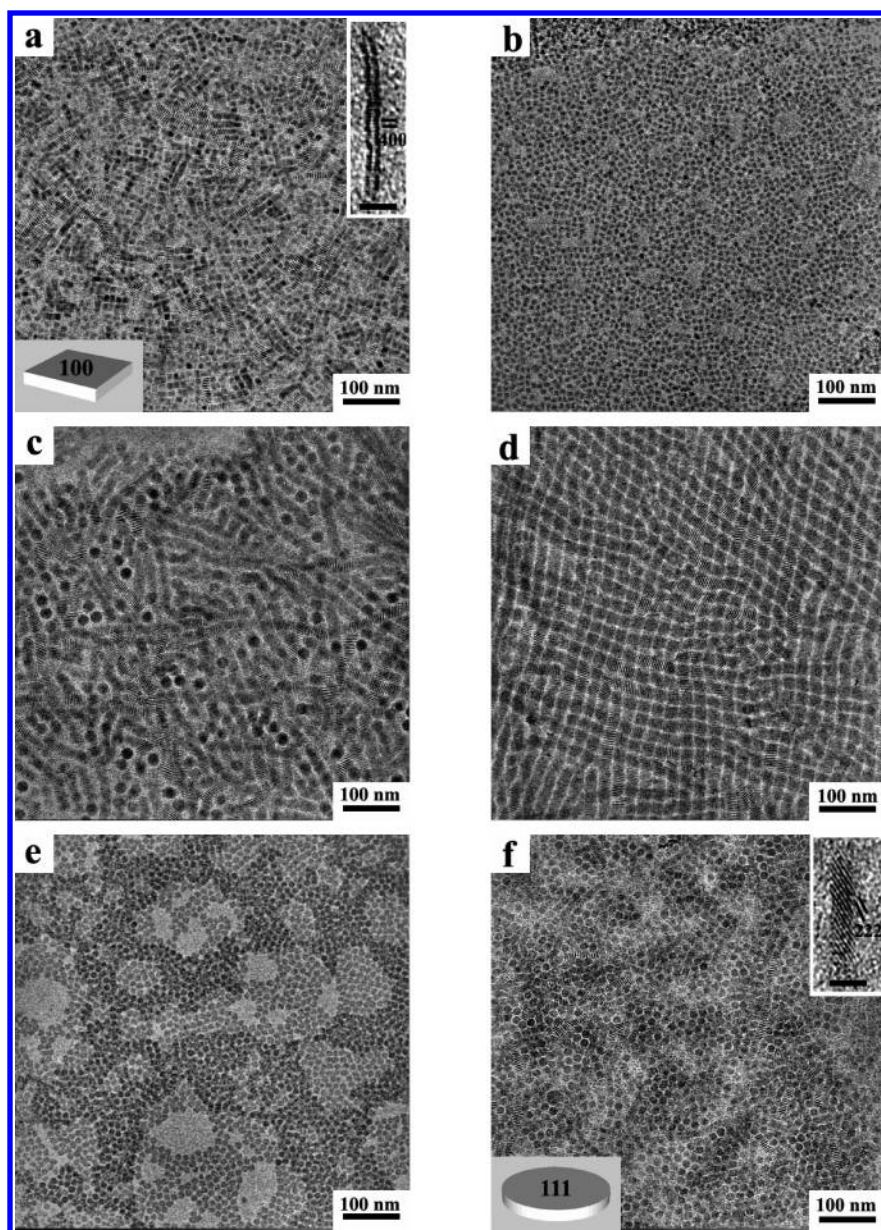

Figure 2. TEM images of the as-obtained RE$_2$O$_3$ nanocrystals: (a) Pr$_2$O$_3$, (b) Nd$_2$O$_3$, (c) Sm$_2$O$_3$, (d) Eu$_2$O$_3$, (e) Ho$_2$O$_3$, and (f) Y$_2$O$_3$. The upper insets in (a) and (f) show the HRTEM images of a Pr$_2$O$_3$ nanoplate and a Y$_2$O$_3$ nanodisk standing on the side surface, respectively (scale bar: 3 nm). The lower insets in (a) and (f) show the schematic diagrams of a RE$_2$O$_3$ nanoplate and a nanodisk, respectively.
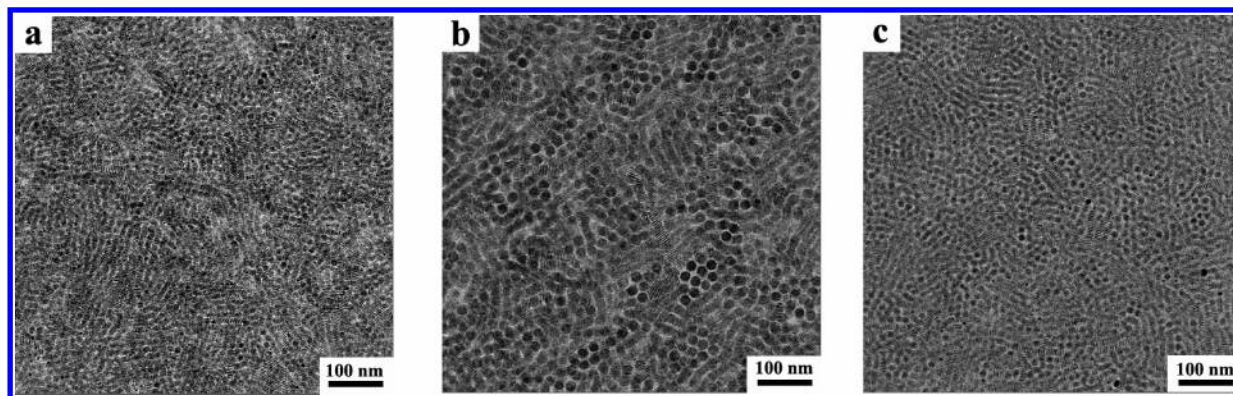
Figure 3. TEM images of the Y_2O_3 nanodisks synthesized under OA/OM/ODE = 2/3/5 at 310 °C for 1 h from 0.5 mmol precursors: (a) $Y(BA)_3$, (b) $Y(Ac)_3$, and (c) $Y(OH)_3$.
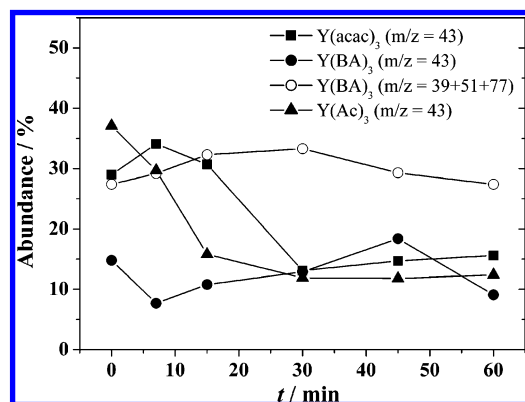

Figure 4. Dependence of the specific m/z abundances on the reaction time (t) during the decomposition of various yttrium precursors.

on the nanocrystal synthesis.

Type of the Precursor: Five kinds of readily available yttrium compounds, including acetylacetonate ($Y(acac)_3$), benzoylacetonate ($Y(BA)_3$), acetate ($Y(Ac)_3$), hydroxide ($Y(OH)_3$), and oxalate ($Y_2(C_2O_4)_3$), were selected as the complex precursors in the present synthesis. It was found that high-quality Y_2O_3 nanodisks could be synthesized from $Y(acac)_3$ (Figure 2f), $Y(BA)_3$ (Figure 3a), $Y(Ac)_3$ (Figure 3b), or $Y(OH)_3$ (Figure 3c) under OA/OM/ODE = 2/3/5 at 310 °C for 1 h (also see Table 1). However, $Y_2(C_2O_4)_3$ did not decompose under the same synthetic conditions. GCMS characterization was utilized to investigate the decomposition kinetics for the former three yttrium complexes.[32] The determined ion fragments for byproducts from the decomposition reaction were the ethoxy cation (CH_3CO^+, m/z = 43; see the Supporting Information, Figure 3Sb,e,h) and/or phenyl cation ($C_6H_5^+$, m/z = 77, 51, 39; see the Supporting Information, Figure 3Se). Figure 4 represents the time dependence of the specific m/z abundances for the above fragments during the decomposition of the precursors. It can be seen that $Y(Ac)_3$ decomposed at a rather high rate in the initial 15 min reaction, whereas $Y(acac)_3$ decomposed rapidly in a reaction lasting 30 min. However, the decomposition of $Y(BA)_3$ progressed slowly throughout the reaction. Thus, the decomposition rate of the yttrium precursors followed the sequence of $Y(Ac)_3 > Y(acac)_3 > Y(BA)_3$, in reverse of the order of their cumulative formation constants (K) of $Y(Ac)_3$ (log K = 3.38) < $Y(acac)_3$ (log K = 13.9) < $Y(BA)_3$ (log K = 20.57).[33] Clearly, the larger the K value, the stronger the coordination interaction between the metal cations and

the ligands and thus the more difficult the decomposition of the metal complex. Herein, we employed the $RE(acac)_3$ precursors, which showed a medium decomposition speed, to prepare the RE_2O_3 nanocrystals.

Concentration of the Precursor: As the concentration of $Y(acac)_3$ was decreased from 0.05 to 0.02 mol L^{-1}, the size of the Y_2O_3 nanodisks was reduced from 13.3 to 10.5 nm, whereas the size-distribution was enlarged from 8 to 17% in S. D. (see Figures 2f and 5a and Table 1). It indicates that the lower concentration of $Y(acac)_3$ resulted in fewer monomers for the growth of Y_2O_3 nanodisks, which showed a size shrinkage via the "defocusing" way.[14]

Solvent Composition: The use of the ternary solvent of OA/OM/ODE was found to be essential for the formation of high-quality Y_2O_3 nanodisks. Without the addition of ODE, only nondispersible, less-uniform Y_2O_3 nanodisks were obtained under OA/OM = 4/6 (see Figure 5b). In pure OM, $Y(acac)_3$ could not be converted into Y_2O_3, whereas in pure OA, the separated solid contained no cubic Y_2O_3. It was also noted that the volume ratio of OA to OM was very important for obtaining high-quality RE_2O_3 nanocrystals under the fixed volume of ODE. When OA/OM was reduced from 2/3 to 1/4, the obtained Y_2O_3 nanodisks showed a smaller size (11.2 nm) (see Figure 5c and Table 1); when OA/OM was increased to 2.5/2.5, the Y_2O_3 nanodisks had a larger size (28.8 nm) (see Figure 5d and Table 1). It seemed that the higher content of OM probably caused a faster nucleation, along with fewer monomers for the nanocrystal growth.

Reaction Temperature (T): Under a fixed precursor concentration of 0.05 mol L^{-1} $Y(acac)_3$, OA/OM/ODE = 2/3/5, and a reaction time of 1 h, as T was decreased from 310 to 290 °C, no solid appeared after the precipitation treatment, indicating an insufficient energy for the decomposition of the precursor to form Y_2O_3. As T was increased to 330 °C, the as-obtained nanocrystals showed a smaller size (12.1 nm) (see Figure 5e and Table 1), possibly due to the formation of a higher concentration of nuclei as well as fewer monomers for the nanocrystal growth at elevated temperature. Therefore, monodisperse Y_2O_3 nanodisks could be obtained at a reaction temperature higher than 310 °C.

Reaction Time (t): Under a fixed precursor concentration of 0.05 mol L^{-1} $Y(acac)_3$, OA/OM/ODE = 2/3/5, and a reaction temperature of 310 °C, as t was shortened from 1 to 0.5 h, the yielded Y_2O_3 nanodisks appeared to be the
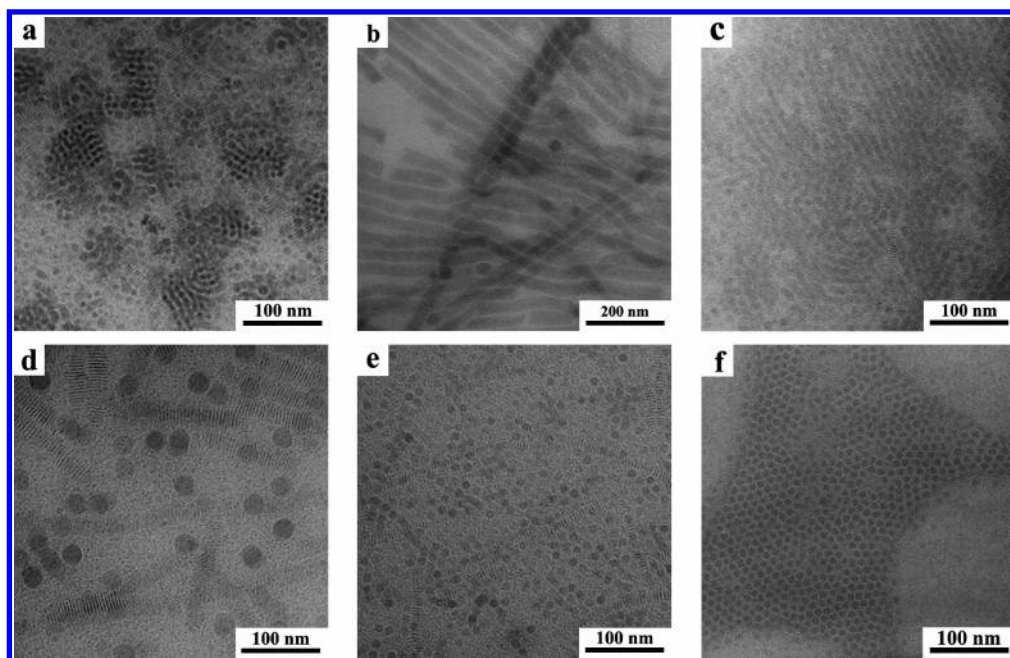
Figure 5. TEM images of the Y_2O_3 nanodisks synthesized under various conditions: (a) 0.2 mmol Y(acac)$_3$, OA/OM/ODE = 2/3/5, 310 °C, 1 h; (b) 0.5 mmol Y(acac)$_3$, OA/OM/ODE = 4/6/0, 310 °C, 1 h; (c) 0.5 mmol Y(acac)$_3$, OA/OM/ODE = 1/4/5, 310 °C, 1 h; (d) 0.5 mmol Y(acac)$_3$, OA/OM/ODE = 2.5/2.5/5, 310 °C, 1 h; (e) 0.5 mmol Y(acac)$_3$, OA/OM/ODE = 2/3/5, 330 °C, 1 h; (f) 0.5 mmol Y(acac)$_3$, OA/OM/ODE = 2/3/5, 310 °C, 0.5 h.

Scheme 1. Hypothesized Formation Mechanism for the RE$_2$O$_3$ Nanoplates and Nanodisks
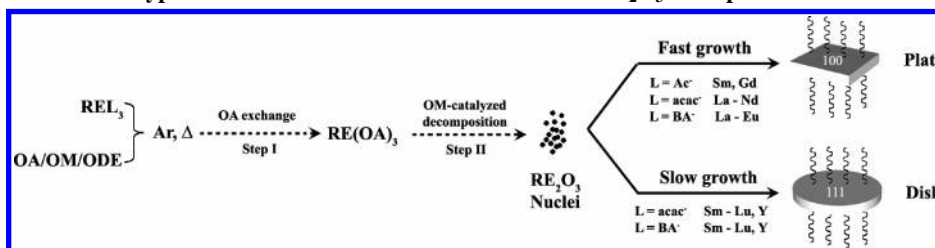
smaller size of 9.4 nm (see Figure 5f and Table 1), suggesting a possible incomplete decomposition of Y(acac)$_3$ in less than 0.5 h. As *t* was prolonged to 2 h, the Y_2O_3 nanodisks had the larger size of 16.7 nm (see Table 1), indicating their continuous growth for reaction times exceeding 1 h. The narrow size distributions (8−10%) for the Y_2O_3 nanodisks were maintained within the 0.5−2 h reaction period.

3. Pathway for the Formation of RE$_2$O$_3$ Nanocrystals. To reveal the mechanism for the transformation from the complex precursors to the RE$_2$O$_3$ nanocrystals, we carried out a detailed TG analysis on the thermo-decomposition of various yttrium complexes. On one hand, the TG runs shown in the Supporting Information, Figure 4Sa−e, indicate that the selected yttrium complexes could not completely be transformed to Y_2O_3 until the heating temperature reached 500 °C. On the other hand, these precursors were observed to decompose in the surfactants at the low temperatures of 230−330 °C by others as well as our group.[9−11,31] Hence, these contradictive results might reveal a totally different mechanism for the formation of RE$_2$O$_3$ nanocrystals in the present work (see Scheme 1). At first, we postulate that a rare-earth oleate (RE(OA)$_3$) intermediate was generated by

the ligand-exchange reaction between REL$_3$ and OA (step I)

$$REL_3 + OA \rightarrow RE(OA)_3 + L \tag{1}$$

In the experiments, the reaction solution became transparent after being heated to ca. 150 °C, indicating the occurrence of the ligand-exchange reaction at this temperature. Previously, Hyeon et al. confirmed such metal-surfactant intermediates during the fabrication of monodisperse transitional metal-oxide nanocrystals and directly used the separated iron-oleate as the precursor for Fe$_2$O$_3$.[5,34] However, as for the rare-earth metals, the separated RE(OA)$_3$ (prepared by the reaction between RE(NO$_3$)$_3$ and NaOA) was unable to produce RE$_2$O$_3$ under the same synthetic conditions as when RE(acac)$_3$ was used as the precursor. Second, the TG results showed that the decomposition of RE(OA)$_3$ did not finish until ca. 400 °C (see the Supporting Information, Figure 4Sf). Therefore, the as-formed RE(OA)$_3$ intermediate should undergo an in situ transformation to RE$_2$O$_3$ catalyzed by the base of OM in the reaction solution (step II)

$$RE(OA)_3 + OM \rightarrow RE_2O_3 + byproducts \tag{2}$$
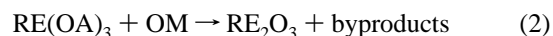
Without the addition of OM, the formation of RE$_2$O$_3$ was

(32) Joo, J.; Yu, T.; Kim, Y. W.; Park, H. M.; Wu, F.; Zhang, J. Z.; Heyon, T. *J. Am. Chem. Soc.* **2003**, *125*, 6553.
(33) Dean, J. A. *Lange's Handbook of Chemistry*, 15th ed.; McGraw-Hill: New York, 1999.

(34) Hyeon, T. *Chem. Commun.* **2003**, 927.

found to end with the remaining $RE(OA)_3$ intermediate. During this step, the RE_2O_3 nuclei were created and underwent subsequent growth with the further release of monomers. Table 1 shows that the minimum ratio between the added OM and $RE(acac)_3$ was decreased from 45 and 49.5 mL mmol^{-1} for the light and middle rare earths (La to Dy) to 6 mL mmol^{-1} for the heavy ones (Ho to Lu, Y). Generally, the basicity of the reaction media should be higher than that of the RE_2O_3 product, otherwise, the above chemical reactions would proceed in the reverse order. Because the basicity of RE_2O_3 decreases from La_2O_3 to Lu_2O_3, the required ratio of OM/$RE(acac)_3$ also decreased across the rare-earth sequence.

4. Shape Evolution of the RE_2O_3 Nanocrystals. The shape control of colloidal nanocrystals has attracted the intensive investigation of many groups.[35−37] Normally, the crystal shape of the inorganic nanocrystals is dependent on the following factors: the crystalline phase of the nuclei, the selective adsorption of surfactant onto specific crystal planes, and the balance between the kinetic and thermodynamic growth regimes.[35−37] For our RE_2O_3 nanocrystals, the crystal phase is cubic, without any structural anisotropy. Therefore, the as-observed 2D growth modes for the RE_2O_3 nanoplates and nanodisks originated from the selective adsorption of surfactant (especially oleic acid, which has a high oxophilicity) onto the specific crystal planes of the RE_2O_3 nanocrystals.[10] However, the shape evolution from the nanoplate to nanodisk across the rare-earth series is quite complex (see Scheme 1). In the present work, as $RE(acac)_3$ was used as the precursors, we have obtained RE_2O_3 nanoplates from La to Nd, and RE_2O_3 nanodisks from Sm to Lu, including Y. Using $RE(BA)_3$ as the precursors in our previous research, a nanoplate shape appeared for those from La_2O_3 to Eu_2O_3, whereas the nanodisk shape formed for those from Sm_2O_3 to Lu_2O_3, including Y_2O_3.[10] As $RE(Ac)_3$ was selected as the precursor, the Gd_2O_3[9] and Sm_2O_3[11] nanoplates were obtained by the other groups. Therefore, we supposed that the studied shape evolution from nanoplate to nanodisk was related to the growth kinetics of various rare-earth oxides synthesized from different precursors.

As is known, the surface density of atoms in the facets of cubic $Ia3$ structure follows {100} > {111}, and thus the order of surface energy for RE_2O_3 is {100} > {111}. When the RE_2O_3 oxide nuclei formed, oleic acid was preferentially adsorbed onto the {100} facets, which would result in a dynamically stable RE_2O_3 nanoplate with the confined growth of the {100} facets. As the reaction temperature was raised and the reaction time was prolonged, the metastable RE_2O_3 nanoplate would be transformed into the thermodynamically stable nanodisk, in which oleic acid was preferentially adsorbed onto the {111} facets. If the RE_2O_3 nuclei underwent a fast growth, the dynamically stable → thermodynamically stable transformation would be restrained, and thus the {100} facet-confined RE_2O_3 nanoplate formed. If

the RE_2O_3 nuclei grew slowly, the above transformation proceeded completely, and the {111} facet-confined RE_2O_3 nanodisk would appear. As revealed by the GCMS analysis, the decomposition rate of $RE(Ac)_3$ was higher than that of $RE(acac)_3$ and $RE(BA)_3$ for the same rare-earth element. According to the previous discussion, the as-formed RE-$(OA)_3$ intermediate was subsequently transformed into RE_2O_3 nuclei with the aid of oleylamine. Therefore, the $Gd(Ac)_3$ and $Sm(Ac)_3$ precursors decomposed to produce Gd_2O_3 and Sm_2O_3 nanoplates under the fast growth mode,[9,11] whereas their acetylacetonate and benzoylacetonate[10] salts generated Gd_2O_3 and Sm_2O_3 nanodisks under the slow growth mode. When the ligand was fixed ($L = acac^-$, BA^-, Ac^-, or OH^-) for the rare-earth complex (REL_3), its cumulative formation constant (K) tends to increase across the rare-earth sequence from La to Lu, and thus its decomposition rate decreased in the OA/OM/ODE solvent.[33] As a result, {100} facet-confined nanoplates were obtained for the light RE_2O_3 (La_2O_3 to Nd_2O_3), and {111} facet-confined nanodisks for the middle and heavy RE_2O_3 (Sm_2O_3 to Lu_2O_3, Y_2O_3), when the precursor was $RE(acac)_3$ or $RE(BA)_3$.

5. Self-Assembly and Surface Modification of RE_2O_3 Nanocrystals. From the TEM images of the Pr_2O_3 nanoplates (Figure 2a), Sm_2O_3 (Figure 2c), and Eu_2O_3 nanodisks (Figure 2d), it can be seen that some nanocrystals self-assembled via their top surfaces to form face-to-face nanoarrays on the TEM grids. Further investigation showed that the dispersant composition had a great effect on the formation of the above self-organized patterns composed of the redispersible RE_2O_3 nanocrystals.[9,10,18] For instance, if the dispersant was pure cyclohexane, most of the 13.3 nm Y_2O_3 nanodisks lay on their bottom surfaces to give a side-to-side pattern (see Figure 6a). As a certain amount of ethanol was added into cyclohexane (cyclohexane/ethanol = 3/1 in volume), nearly all the nanodisks stood on their side surfaces to appear in a face-to-face pattern (see Figure 6b). If further increasing the volume fraction of ethanol to 1/1, the solution became turbid with the formation of nanodisk precipitate.

Generally speaking, the self-assembly of colloidal inorganic nanocrystals on the 2D substrate is largely dependent on multiple factors, including the monodispersity, shape and surface-adsorption feature of the nanocrystals, the type of the substrate, and the fabrication conditions (concentration of nanocrystals, ambient temperature and humidity, etc.).[20−29] In our experiments, we fixed the carbon-coated copper grid as the hydrophobic substrate and tried to keep the fabrication conditions constant for each TEM sample. Rationally, the as-observed alteration of the self-assembly patterns should be related to the nature of the redispersible RE_2O_3 nanocrystals. To understand the self-assembly behavior of the present RE_2O_3 nanocrystals, we suggested the possible interparticle interaction modes for the OA-capped RE_2O_3 nanodisks in various dispersants, which are simply depicted in Scheme 2.

As for the RE_2O_3 nanodisks, the oleic acid was mainly adsorbed onto their top and bottom surfaces. The exposed hydrophobic alkyl groups were well-immersed in the nonpolar solvent (e.g., cyclohexane) and guaranteed the good dispersibility of the nanodisks. The capped OA ligand

(35) Manna, L.; Scher, E. C.; Alivisatos, A. P. *J. Cluster Sci.* **2002**, *13*, 521.

(36) Burda, C.; Chen, X.; Narayanan, R.; El-Sayed, M. A. *Chem. Rev.* **2005**, *105*, 1025.

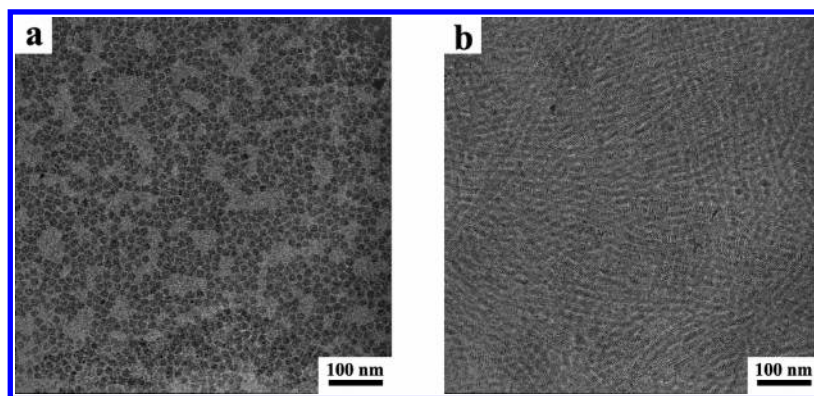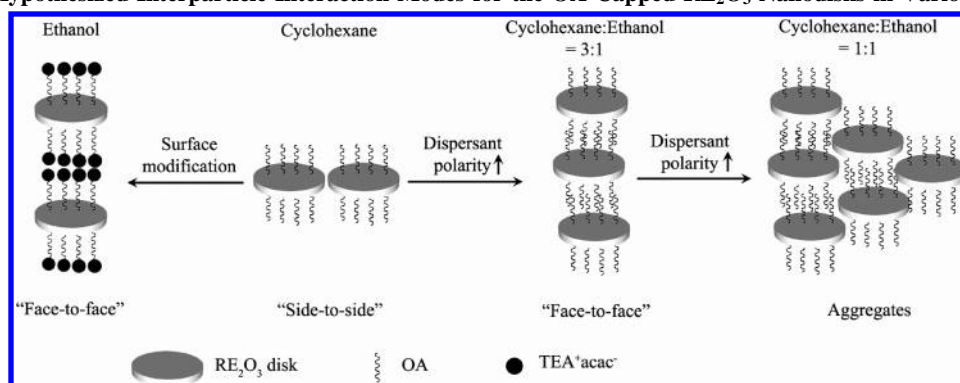(37) Jun, Y.-W.; Choi, J.-S.; Cheon, J. *Angew. Chem., Int. Ed.* **2006**, *45*, 3413.

Figure 6. TEM images of the as-obtained Y_2O_3 nanodisks re-dispersed in (a) cyclohexane and (b) cyclohexane/ethanol (3/1 in v/v).

Scheme 2. Hypothesized Interparticle Interaction Modes for the OA-Capped RE_2O_3 Nanodisks in Various Dispersants

prevented the as-obtained nanocrystals from self-aggregation via the interparticle dipolar—dipolar repulsive forces. Therefore, the RE_2O_3 nanodisks lay down on the substrate via their bottom surfaces in order to reduce their total energy as deposited. As the polarity of the dispersant increased with the addition of ethanol, the interfacial tension increased and the alkyl groups were partly immersed in the solvent. Under this condition, the capped OA ligand tended to be compacted by the polar ethanol solvent, and they were thus intertwined with each other. Therefore, the deposited RE_2O_3 nanodisks tended to be aligned via the face-to-face formation and stood up on the substrate via the side surface so as to minimize their total energy. As the polarity of the dispersant further increased, the alkyl groups of OA could not be immersed in the high polar solvent, and thus the nanodisks were severely aggregated (see right half of Scheme 2).

Figure 7 shows the size distributions of the different Y_2O_3 nanodisk dispersions determined by dynamic light scattering
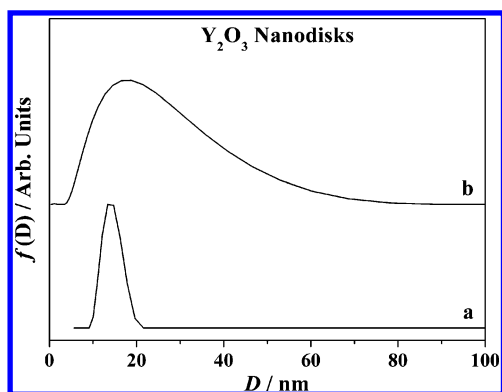

Figure 7. DLS size-distributions of the as-obtained Y_2O_3 nanodisks redispersed in (a) cyclohexane and (b) cyclohexane/ethanol (3/1 in v/v).

(DLS) experiments. The mean micellar size of the cyclohexane dispersible nanodisks was 14.0 nm, very close to the TEM value of 13.3 nm (see Table 1), with a narrow size distribution of S. D. = 2.1%. Thus, it indicates that the nanodisks exist as discrete entities in cyclohexane. The mean micellar size of the nanodisks dispersed in cyclohexane/ ethanol (3/1 in volume) was increased to 17.7 nm, and the relevant size distribution (S. D. = 6.2%) was also broader. It reveals that the nanodisks partly aggregated as the polarity of the dispersant increased. Therefore, the present results have shown that the self-assembly of dispersible nanocrystals might occur in the solution phase as well as during the dynamic evaporation of solvent on certain substrates.[29]

To make the as-obtained RE_2O_3 nanocrystals redispersible in polar solvents (e.g., ethanol), we have designed a simple surface-modification process (see the left side of Scheme 2). The triethylammonium cation (TEA^+) was set to bond the capped OA ligands via the hydrophobic interaction. The acetylacetonate anion ($acac^-$) was then fixed to the TEA^+ ion via the electrostatic attraction. Thus, the surface-modified nanocrystals were exposed with the hydrophilic diketonate groups and could be redispersed in ethanol. Figure 8 is the TEM image of the ethanol-dispersible Y_2O_3 nanodisks. The surface-modified nanocrystals maintained their size and shape and aligned via their side surfaces to form face-to-face nanoarrays.

6. Optical Properties of the Y_2O_3:Eu Nanodisks. By the simultaneous thermolysis of multiple rare-earth acetylacetonate precursors, high-quality composite RE_2O_3 nanocrystals could be synthesized. Experimentally, cubic Y_2O_3:Eu (5 at %) nanodisks were prepared from stoichiometric $Y(acac)_3$ and $Eu(acac)_3$ in OA/OM/ODE (see Table 1). The size of
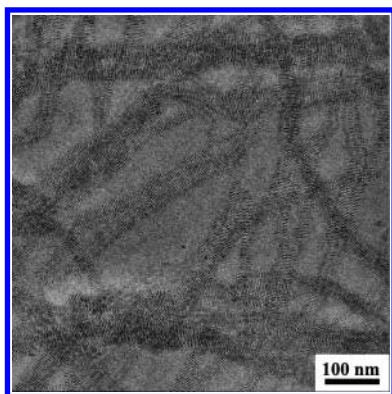
Figure 8. TEM image of the ethanol-dispersible Y_2O_3 nanodisks.

the Y_2O_3:Eu nanodisks could be tuned from 16.0 (Figure 9a) to 23.2 nm (Figure 9b). For comparison, we selected the commercial Y_2O_3:Eu (5 at %) powder as the bulk reference and the Y_2O_3:Eu (5 at %) nanoparticles in the size of ca. 40 nm (see the Supporting Information, Figure 5S), prepared via the a coprecipitation route, as the nanoparticle reference.

Excitation Spectra: Figure 10a (left part) represents the room-temperature excitation spectra of the Y_2O_3:Eu samples. The bands at the wavelength of 240−290 nm can be ascribed to the charge-transfer (CT) transition from O^{2-} 2p to Eu^{3+} 4f orbital, which is related to the covalency, i.e., the red shift in the CT band refers to the increase in the covalency between oxygen and europium atoms.[38,39] Clearly, the CT bands of the nanodisk samples (**Y1** and **Y2**) show a distinct red shift, compared with those of the nanoparticle (**Y3**) and bulk references (**Y4**). This red shift may be caused by the capped OA ligand, which effectively increased their covalent bonding to the surface Eu^{3+} ions for the nanodisks.

Emission Spectra: Figure 10a (right part) shows the room-temperature emission spectra of the Y_2O_3:Eu samples. The bands in the wavelength of 550−750 nm can be described by the $^5D_0 \rightarrow {}^7F_j$ line emissions ($J = 0, 1, 2, 3,$ and 4) of the Eu^{3+} ion.[40] Because the spectral shapes for the nanodisks with different sizes of 16.0 (**Y1**) and 23.2 nm (**Y2**) show little discrepancy, no obvious size effect can be determined for the fluorescence emission of the Y_2O_3:Eu nanodisk. A striking feature is that the intensity ratio of the peak at 625 nm to the peak at 610 nm in the $^5D_0 \rightarrow {}^7F_2$ emission is greatly increased for the nanodisk, compared with that for the nanoparticle (**Y3**) and bulk (**Y4**) references. For the line

emissions of the Eu^{3+} ion, the $^5D_0 \rightarrow {}^7F_1$ and $^5D_0 \rightarrow {}^7F_2$ bands correspond well to the orange-red and red color, respectively. Hence, the intensity ratio of $^5D_0 \rightarrow {}^7F_2$ to $^5D_0 \rightarrow {}^7F_1$ is equal to the red/orange (*R/O*) ratio.[41] For our Y_2O_3: Eu nanodisk, the calculated *R/O* value was 9.4 for the 16.0 nm sample and 7.8 for the 23.2 nm sample, distinctly higher than those for the nanoparticle (7.1) and bulk (6.2) references. Therefore, the Y_2O_3:Eu nanodisks obtained in this work could emit highly pure red light.

Site-Selective Excited Emission Spectra: Previously, we have reported the above unusual emission of the 625 nm peak for the undoped Eu_2O_3 nanodisks and attributed it to the higher fraction of surface Eu^{3+} ion in the 2D growth structure of the nanodisk, which was composed of six {111} layers with a thickness of only 1.6 nm.[10] Herein, the site-selective excited emission technique was carried out to probe the real symmetric site of Eu^{3+} ion in the Y_2O_3:Eu nanodisks.

Figure 10b is the excitation spectra of the Y_2O_3:Eu nanodisk (**Y2**) and the bulk reference (**Y4**) under the emission wavelength of 625 nm. The peaks located at 581.1 and 580.7 nm can be assigned to the $^5D_0 \rightarrow {}^7F_0$ transition for the Y_2O_3:Eu nanodisk sample and bulk reference, respectively. The site-selective emission spectra were measured at 77 K using different resonant excitation wavelengths into the $^5D_0 \rightarrow {}^7F_0$ absorption bands, labeled by the arrows in Figure 10b with numbers S_1 to S_3 for the nanodisk and S_1' to S_3' for the bulk sample. Figure 10c shows that the identical emission spectra with two peaks at ca. 614 and 623 nm appeared for the nanodisk sample under the different excitation wavelength of S_1 (581.1 nm), S_2 (581.4 nm), or S_3 (581.9 nm). This indicates that the Eu^{3+} ion in the nanodisk took only one symmetric site. As for the bulk reference, Figure 10d shows that the emission spectra were nearly equal with a strong peak at 611 nm and a weak peak at 631 nm, under the excitation wavelength of S_1' (580.7 nm), S_2' (581.9 nm), or S_3' (582.3 nm). This suggests that there is only one symmetric site for the Eu^{3+} ion in the bulk reference with a cubic phase.[42,43]

Compared with the bulk reference, the Eu^{3+} ions in the Y_2O_3:Eu nanodisks totally displayed a surface symmetric site. Furthermore, this new site differed from that in the reported bulk Y_2O_3:Eu with a monoclinic phase.[44,45] Actually, the enhanced emission of the 625 nm peak for the cubic (*Ia*3) Y_2O_3:Eu nanodisks is just like that for the nanostructured
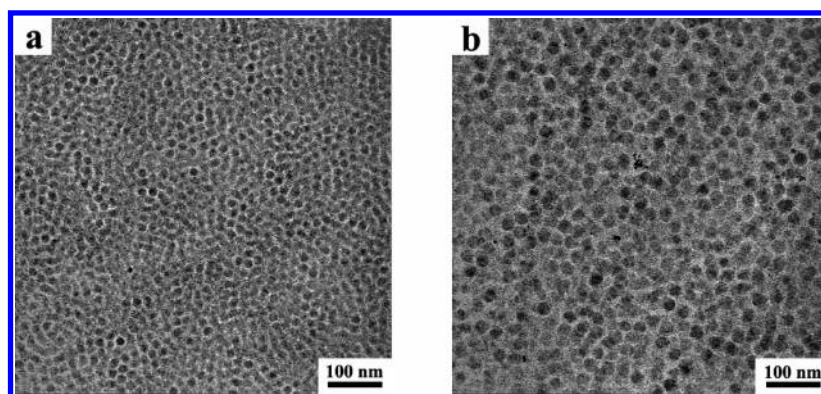

Figure 9. TEM images of the Y_2O_3:Eu (5 at %) nanodisks synthesized from stoichiometric Y(acac)$_3$ and Eu(acac)$_3$ precursors at 310 °C for 1 h under (a) OA/OM/ODE = 3/4.5/2.5 and (b) OA/OM/ODE = 4/6/0.

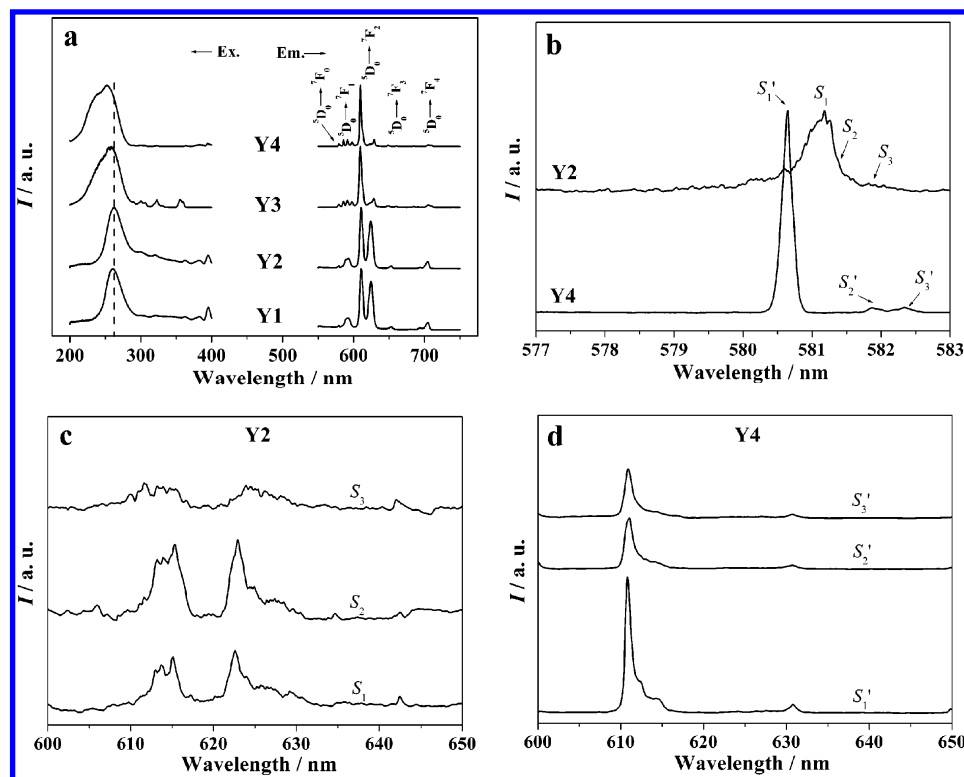**Figure 10.** (a) Room-temperature fluorescence spectra of the Y_2O_3:Eu (5 at%) samples: **Y1**, 16.0 nm nanodisk (λ_{em} = 612 nm, λ_{ex} = 263 nm); **Y2**, 23.2 nm nanodisk (λ_{em} = 610 nm, λ_{ex} = 263 nm); **Y3**, 40 nm nanoparticle prepared by a coprecipitation method (λ_{em} = 610 nm, λ_{ex} = 260 nm); **Y4**, commercial powder (λ_{em} = 610 nm, λ_{ex} = 253 nm). (b) Excitation spectra of **Y2** and **Y4** under 625 nm emission at 77 K. (c) Emission spectra of **Y2** under S_1 (581.1 nm), S_2 (581.4 nm), and S_3 (581.9 nm) excitation at 77 K. (d) Emission spectra of **Y4** under S_1' (580.7 nm), S_2' (581.9 nm), and S_3' (582.3 nm) excitation at 77 K.

mesoporous materials with a monoclinic phase and a small confined thickness of 0.6 nm.[46] On the basis of these results, we can draw a conclusion that the Eu^{3+} ions around and inside the nanodisk took a unique symmetry site due to the ultrathin thickness of the nanodisk, different from that in the bulk Y_2O_3:Eu with the cubic or monoclinic structure.

Conclusions

High-quality RE_2O_3 ultrathin nanoplates and nanodisks were obtained via a nonhydrolytic approach in OA/OM/ODE using several kinds of rare-earth complexes, including acetylacetonate, benzoylacetonate, and acetate, as the precursors. The RE_2O_3 nanocrystals seemed to result from a two-step reaction, i.e., the ligand-exchange reaction between the complex salts and oleic acid, followed by the oleylamine-catalyzed decomposition of the rare-earth oleate intermediate. The dynamically stable nanoplate and thermodynamically stable nanodisk could be controllably synthesized for various rare-earth elements under fast/slow growth modes. Two types of self-assembly nanoarrays (side-to-side and face-to-face) appeared on the TEM grids for the as-obtained nanocrystals redispersed in different dispersants. The high-quality Y_2O_3: Eu nanodisks were identified to hold a new symmetric site for the Eu^{3+} ion, as compared with its bulk reference, and thus showed surface-dependent, highly pure red emissions, which might benefit the application in nanodevices. In summary, the present controlled synthesis has several merits of good reproducibility, low cost, and easy operation and contributes a lot to the development of synthetic strategy, size- and shape-control theory, and self-assembly principles for the dispersible inorganic nanocrystals (especially metal oxide nanocrystals).

Supporting Information Available: Elementary analyses of C, H contents in the rare-earth acetylacetonate complexes (Table 1S), XRD patterns of the as-dried RE_2O_3 nanocrystals (Figure 1S), TEM images of the as-obtained RE_2O_3 nanocrystals (Figure 2S), GCMS spectra for the gaseous byproducts from the thermolysis of rare earth complexes (Figure 3S), TG curves of the selected yttrium complexes (Figure 4S) and TEM image of the Y_2O_3:Eu (5 at %) nanoparticles (Figure 5S) (PDF). This material is available free of charge via the Internet at http://pubs.acs.org.

CM0618392

(38) Su, Q. *Inorg. Mater.* **1987**, *2*, 1.
(39) Pei, Z.; Su, Q.; Li, S. *J. Lumin.* **1991**, *50*, 123.
(40) Blasse, G.; Grabmaier, B. C. *Luminescent Materials*; Springer: Berlin, 1994.
(41) Wei, Z.-G.; Sun, L.-D.; Liao, C.-S.; Yin, J.-L.; Jiang, X.-C.; Yan, C.-H.; Lü, S.-Z. *J. Phys. Chem. B* **2002**, *106*, 10610.
(42) Williams, D. K.; Yuan, H.; Tissue, B. M. *J. Lumin.* **1999**, *83–84*, 297.
(43) Yin, M.; Duan, C.; Zhang, W.; Lou, L.; Xia, S.; Krupa, J. C. *J. Appl. Phys.* **1999**, *86*, 3751.
(44) Bihari, B.; Eilers, H.; Tissue, B. M. *J. Lumin.* **1997**, *75*, 1.
(45) Williams, D. K.; Bihari, B.; Tissue, B. M.; McHale, J. M. *J. Phys. Chem. B* **1998**, *102*, 916.
(46) Pinna, N.; Garnweitner, G.; Beato, P.; Niederberger, M.; Antonietti, M. *Small* **2005**, *1*, 112.